Computational Methods in Applied Sciences

Sergio R. Idelsohn *Editor*

Numerical Simulations of Coupled Problems in Engineering

ECCOMAS
European Community on Computational Methods in Applied Sciences

Springer

Numerical Simulations of Coupled Problems in Engineering

Computational Methods in Applied Sciences

Volume 33

Series editor

E. Oñate
International Center for Numerical Methods in Engineering (CIMNE)
Technical University of Catalonia (UPC)
Edificio C-1, Campus Norte UPC
Gran Capitán, s/n
08034 Barcelona, Spain
e-mail: onate@cimne.upc.edu
url: http://www.cimne.com

For further volumes:
http://www.springer.com/series/6899

Sergio R. Idelsohn
Editor

Numerical Simulations of Coupled Problems in Engineering

Springer

Editor
Sergio R. Idelsohn
International Center for Numerical
Methods in Engineering (CIMNE)
Catalan Institution for Research
and Advanced Studies (ICREA)
Barcelona
Spain

ISSN 1871-3033
ISBN 978-3-319-06135-1 ISBN 978-3-319-06136-8 (eBook)
DOI 10.1007/978-3-319-06136-8
Springer Cham Heidelberg New York Dordrecht London

Library of Congress Control Number: 2014939045

Printed on acid-free paper

Springer is part of Springer Science+Business Media (www.springer.com)

Preface

This book contains state-of-the-art contributions in the field of Coupled Problems in Engineering. A selected specialist has written each chapter as an extended version of the paper presented at the conference "Fifth Computational Methods for Coupled Problems in Science and Engineering" held in Ibiza in July 2013. This Conference brought together more than 400 participants from 41 countries and was dedicated to celebrate the 60th birthday of Prof. Eugenio Oñate.

The Conference was included as one of the Thematic Conferences of the European Community on Computational Methods in Applied Sciences (ECCOMAS) and a Special Interest Conference of the International Association for Computational Mechanics (IACM). It was also supported by other scientific organizations in Europe and worldwide.

This book contains 16 chapters written by distinguished authors, who present and discuss mathematical models, numerical methods, and computational techniques for solving Coupled Problems of multidisciplinary character. The goal of this book is to take a step forward in the formulation and solution of real life problems with a multidisciplinary vision, accounting for all the complex couplings involved in the physical description of the problem.

Topics treated in the various chapters include developments and applications of Coupled Problems in a wide variety of situations such as Non-Linear Materials, Cardiovascular Fluid Mechanics, Multi-Fluid Flows, or Fluid-Structure Interactions, using different techniques like particle methods, reduced order models or partitioned parallelization techniques.

This book includes contributions submitted directly by authors. The editor cannot accept responsibility for any inaccuracies, comments, and opinions contained in the text.

The editor would like to take this opportunity for thanking all authors for submitting their excellent contributions on time. Many thanks also to ECCOMAS and Springer for accepting the publication of this book in the series "Computational Methods in Applied Sciences."

Sergio R. Idelsohn

Contents

Part VII Partitioned Method and Parallelization Techniques

Part I
Non-Linear Materials in Coupled Problems

Generalized Viscoplasticity Based on Overstress (GVBO) for Large Strain Single-Scale and Multiscale Analyses

Vasilina Filonova, Yang Liu and Jacob Fish

Abstract A generalized viscoplasticity based on the overstress (GVBO) model that successfully reproduces large strain and strain rate experimental data has been developed. The GVBO model confirmed increased shear resistance of polyurea at very high strain rates (10^5–$10^6\ s^{-1}$) observed in the experiments. With the proposed GVBO model, we conducted numerical simulation of fragment simulating projectile impacting polyurea/ high-hard-steel bi-layers at high impact velocities (>1000 m/s). For model validation, two positions of the polymer coating with respect to the steel plate have been considered: the front and back coating, with a front side being a target. Numerical impact simulations utilizing a single-scale GVBO model predicted that a polyurea bi-layer with a front coating increases penetration velocity by about 15.4 % (against 23 % observed in the experiments), while the steel plate with a back coating raises penetration velocity by 7.5 % (as opposed to 8.8 % in the experiment) in comparison to the ballistic limit of the blank steel plate. This minor discrepancy between experimental and simulation results is qualitatively attributed to the space-time multiscale phenomena. We show that a possible anisotropy introduced by material heterogeneity increases resistance of the polyurea layer by partially transforming the pressure wave into a dissipated shear wave. We further demonstrate that dispersion further enhances energy absorption of the polyurea coating.

Keywords Polyurea · Viscoplasticity model based on the overstress · Multiscale · Anisotropy · Dispersion

V. Filonova · Y. Liu · J. Fish (✉)
Columbia University, Newyork, USA
e-mail: fishj@columbia.edu

S. R. Idelsohn (ed.), *Numerical Simulations of Coupled Problems in Engineering*,
Computational Methods in Applied Sciences 33, DOI: 10.1007/978-3-319-06136-8_1,

1 Introduction

The present manuscript focusses on a single-scale and multiscale modeling of copolymers. A copolymer is a polymer derived from two (or more) monomeric species, as opposed to a homopolymer where only one monomer is used. Polyurea, which is a generic term for a block copolymer, comprises of homopolymer subunits linked by covalent bonds. The union of the homopolymer subunits may require an intermediate non-repeating subunit, known as a junction block. Polyurea exhibits a wide range of mechanical properties, from soft rubber to hard plastic depending on the chemistry. The range of properties together with their rapid reaction has led to many applications as coatings, for example on tunnels, bridges, roofs, parking decks, storage tanks, freight ships, truck beds, etc. Polyurea coatings have been applied to military armor to increase its resistance to ballistic penetration [1].

Many copolymer models [2–6] are derived from the standard linear solid model (SLS), capable of predicting both creep and relaxation as shown in Fig. 1.

The arm 1 in Fig. 1 is a hyperelastic arm, whereas the bottom arm in Fig. 1 is the Maxwell arm consisting of a dashpot and hyperelastic spring connected in series. For large strain problems [5, 6], the deformation gradient in the bottom arm, $\mathbf{F}_2 = \mathbf{F}_1 \equiv \mathbf{F}$, which is identical to the deformation gradient in the top arm, is decomposed into elastic and inelastic deformation gradients

$$\mathbf{F}_2 = \mathbf{F}_2^e \mathbf{F}_2^{in} \tag{1}$$

The elastic response in the hyperelastic arm is assumed to obey Neo-Hookean law, whereas the stress in the Maxwell arm $\boldsymbol{\sigma}_2$ depends on left stretch tensor $\mathbf{V}_2^e$ and pressure p_2 in the Maxwell arm, i.e. $\boldsymbol{\sigma}_2 = f\left(\mathbf{V}_2^e, p_2\right)$. For more details we refer to [5, 6]. These models, however, have been considered for up to the strain rates of $10^4\,\mathrm{s}^{-1}$.

The primary objectives of the present chpater are as follows:

- Develop a block copolymer constitutive model for large strains and strain rates in the range of 10^5–$10^6\,\mathrm{s}^{-1}$. Rather than utilizing the framework of multiplicative decomposition (1), we will pursue an additive decomposition of the rate of deformation

$$\mathbf{D} = \mathbf{D}^e + \mathbf{D}^{in} \tag{2}$$

  The evolution of the inelastic responses will follow the framework of the VBO model [7, 8] with only exception that the elastic constants and viscosity will be assumed to be deformation-dependent. While there are a number of available models of polyurea in the literature [9], to our knowledge, there is no published work utilizing the framework of viscoplasticity model based on overstress (VBO) to describe exceedingly large strains and strain rates observed in the experiments. In the following we will refer to the generalization of the VBO model to large strains and strain rates as the GVBO.

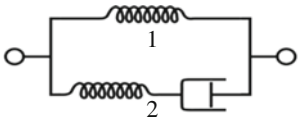

Fig. 1 Rheological model of the polymer. Arm 1—spin model, arm 2—Maxwell arm consisting of spring and dashpot

- Validate the proposed GVBO constitutive model. We will consider recent experiments conducted at Brown University (impact of a steel flyer on a steel/polyurea/steel sandwich plate under high shear strain rates) [10–12].
- Validate the GVBO model on the structural impact problem. We will consider the impact of the projectile onto the polyurea/steel bi-layer where a polymer layer is placed on the front or back of the plate. We will verify experimental observation suggesting considerable advantage of placing the polyurea layer on the top of the target plate at very high impact velocities (>1000 m/s) [13–15]. It is noteworthy to point out that for low to moderate impact velocities the back polyurea coating of the plate shows better resistance than the front coating [16].
- The last part of the manuscript will consider space-time multiscale analysis of the block copolymer to explain some of the discrepancies of the single-scale GVBO model. The polyurea microstructure will be modeled as a two-phase heterogeneous anisotropic material with the inclusion phase being elastic and the soft domains obeying GVBO constitutive model. The multiple temporal scale effect, which gives rise to dispersion, will be taken into account using the recently developed micro-inertia approach [17].

2 Generalized Viscoplasticity Based on Overstress (GVBO) for Large Strains

In this section we present the generalized viscoplasticity model based on overstress (GVBO) for large strain and strain rate problems. First, in Sect. 2.1, the model is stated in the corotational (or rotation-free) frame. Subsequently, in Sects. 2.2 and 2.3, we develop a deformation-dependent elastic modulus and viscosity function for the classical VBO model [7, 8].

2.1 VBO for Large Rotations

We start form the constitutive equation based on the additive decomposition of the rate of deformation

$$\overset{\circ}{\boldsymbol{\sigma}} = \mathbf{L} : \left(\mathbf{D} - \mathbf{D}^{in}\right) \tag{3}$$

where $\overset{\circ}{\boldsymbol{\sigma}}$ is an objective Cauchy stress rate; $\mathbf{D}$ is the rate of deformation tensor, and $\mathbf{D}^{in}$ is the inelastic rate of deformation. The elastic constitutive tensor $\mathbf{L}$ for isotropic material is given by

$$\mathbf{L} = \lambda \mathbf{1} \otimes \mathbf{1} + 2G\mathbf{I} \tag{4}$$

where λ is the first Lame constant, and G is the shear modulus.

To account for large rotations, we consider the Green-Naghdi rate of Cauchy stress, which describes material response in the initial rotation-free frame. The Green-Naghdi rate of the Cauchy stress is defined by

$$\overset{\circ}{\boldsymbol{\sigma}} = \dot{\boldsymbol{\sigma}} + \boldsymbol{\sigma}\left(\dot{\boldsymbol{R}}\boldsymbol{R}^{T}\right) - \left(\dot{\boldsymbol{R}}\boldsymbol{R}^{T}\right)\boldsymbol{\sigma} \tag{5}$$

The flow rule for the case of finite rotations but small strains is given by

$$\mathbf{d} = \mathbf{d}^{e} + \mathbf{d}^{in} = \frac{1+\nu}{E}\overset{\circ}{\mathbf{s}} + \frac{3}{2}\frac{\mathbf{s}-\mathbf{g}}{Ek} \tag{6}$$

where $\mathbf{d}$ is the deviatoric part of the rate of deformation tensor $\mathbf{D}$ decomposed into elastic and inelastic parts, $\mathbf{d}^{e}$ and $\mathbf{d}^{in}$, respectively. $\mathbf{s}$ is the deviatoric Cauchy stress tensor; $\mathbf{g}$ is the deviatoric part of the equilibrium stress; E is the Young's modulus; ν is the Poisson's ratio, and k is the viscosity function defined as

$$k = k_1\left(1 + \frac{\Gamma}{k_2}\right)^{-k_3} \tag{7}$$

where k_1, k_2, k_3 are material constants. The overstress invariant is defined by

$$\Gamma = \sqrt{\frac{2}{3}(\mathbf{s}-\mathbf{g}) : (\mathbf{s}-\mathbf{g})} \tag{8}$$

The evolution law for the equilibrium stress is given by

$$\overset{\circ}{\mathbf{g}} = \frac{\psi}{E}\left(\overset{\circ}{\mathbf{s}} + \frac{\mathbf{s}-\mathbf{g}}{k} - \frac{\Gamma}{k}\frac{(\mathbf{g}-\mathbf{f})}{A}\right) + \left(1 - \frac{\psi}{E}\right)\overset{\circ}{\mathbf{f}} \tag{9}$$

where ψ is the shape function defined as

$$\psi = a_1 + (a_2 - a_1)\exp(-a_3\Gamma) \tag{10}$$

with a_1, a_2, a_3 being material constants.

The evolution laws of the kinematic stress function $\overset{\circ}{\mathbf{f}}$ is defined as

$$\overset{\circ}{\mathbf{f}} = \bar{E}_t\frac{\mathbf{s}-\mathbf{g}}{Ek}; \quad \bar{E}_t \equiv \frac{2}{3}\frac{E_t}{(1 - E_t/E)} \tag{11}$$

and of the isotropic stress function $\dot{A}$ as

$$\dot{A} = A_c \left(A_f - A\right) \frac{\Gamma}{Ek}; \quad A[t=0] = A_0 \tag{12}$$

where A_c, A_f are material constants.

For more details about the classical VBO model see [7, 8].

2.2 Deformation-Dependent Elastic Constitutive Tensor

We introduce the following deformation-dependent Lame constants related to small strain elastic constitutive tensor (4)

$$\begin{aligned} \lambda[J] &= J^p \lambda_0 \\ G[J] &= J^p \left(G_0 - \lambda_0 \ln J\right) \end{aligned} \tag{13}$$

where λ_0, G_0 are the initial (small deformation) values and p is a material parameter; the Jacobian is defined as usual by $J = \det(\mathbf{F})$ where $\mathbf{F}$ is the deformation gradient tensor. The elastic constitutive tensor (4) is assumed to be a function of the Jacobian

$$\mathbf{L}[J] = \lambda[J]\mathbf{1} \otimes \mathbf{1} + 2G[J]\mathbf{I} \tag{14}$$

The initial elastic properties E_0, ν_0 are related to the initial Lame constants by

$$\lambda_0 = \frac{E_0 \nu_0}{(1+\nu_0)(1-2\nu_0)}; \quad G_0 = \frac{E_0}{2(1+\nu_0)} \tag{15}$$

The deformation-dependent Young's modulus and Poisson ratio are related to deformation-dependent Lame parameters (13) by

$$E[J] = \frac{G[J]\left(3\lambda[J] + 2G[J]\right)}{\lambda[J] + G[J]}; \quad \nu[J] = \frac{\lambda[J]}{2\left(\lambda[J] + G[J]\right)} \tag{16}$$

The elastic parameters are allowed to increase only from their initial values: $G \geq G_0$, $\lambda \geq \lambda_0$, $E \geq E_0$; i.e. if elastic parameters decrease based on Eq. (13), the initial values are taken instead.

2.3 The Deformation-Dependent Viscosity Function

We assume the viscosity k to be a function of overstress and Jacobian as follows

Table 1 Generalized VBO model summary

GVBO	Parameters 15: E_0, ν_0, E_t, p, a_1, a_2, a_3, k_1, k_2, k_3, k_4, E_m, A_0, A_c, A_f
Elastic moduli	$E[J] = \frac{G[J](3\lambda[J]+2G[J])}{\lambda[J]+G[J]}$ $\lambda[J] = J^p\lambda_0; \quad G[J] = J^p\,(G_0 - \lambda_0 \ln J)$ $\lambda_0 = \frac{E_0\nu_0}{(1+\nu_0)(1-2\nu_0)}; \quad G_0 = \frac{E_0}{2(1+\nu_0)}$
Flow law	$\mathbf{d} = \frac{1+\nu}{E[J]}\overset{\circ}{\mathbf{s}} + \frac{3}{2}\frac{\mathbf{s}-\mathbf{g}}{E[J]k[\Gamma,J]}$
Equilibrium stress evolution law	$\overset{\circ}{\mathbf{g}} = \frac{\psi}{E[J]}\left(\overset{\circ}{\mathbf{s}} + \frac{\mathbf{s}-\mathbf{g}}{k[\Gamma,J]} - \frac{\Gamma}{k[\Gamma,J]}\frac{(\mathbf{g}-\mathbf{f})}{A}\right) + \left(1 - \frac{\psi}{E[J]}\right)\overset{\circ}{\mathbf{f}}$
Kinematic stress evolution law	$\overset{\circ}{\mathbf{f}} = \bar{E}_t[J]\frac{\mathbf{s}-\mathbf{g}}{E[J]k[\Gamma,J]}; \quad \bar{E}_t[J] \equiv \frac{2E_t}{3(1-E_t/E[J])}$
Isotropic stress function evolution law	$\dot{A} = A_c\,(A_f - A)\,\frac{\Gamma}{E[J]k[\Gamma,J]}; \quad A\,(t=0) = A_0$
Shape function	$\psi = a_1 + (a_2 - a_1)\,e^{-a_3\Gamma}$
Viscosity function	$k[\Gamma, J] = k_1\left(1 + \frac{\Gamma}{\bar{k}_2[J]}\right)^{-k_4}; \quad \bar{k}_2[J] \equiv k_2 + k_3\frac{E[J]-E_0}{E_m-E_0}$

$$k[\Gamma, J] = k_1\left(1 + \frac{\Gamma}{\bar{k}_2[J]}\right)^{-k_4}; \quad \bar{k}_2[J] \equiv k_2 + k_3\frac{E[J]-E_0}{E_m-E_0} \tag{17}$$

where k_1, k_2, k_3, k_4, E_m are material parameters. Note that $\bar{k}_2 = k_2$ is constant when Young's modulus is constant, i.e. the deformation is small. The parameter E_m is a maximum Young's modulus and k_3 defines the sensitivity to large deformation.

The generalized VBO model for the finite deformation theory is summarized in Table 1.

3 Model Validation

3.1 Experimental Setup

The experiments investigating resistance of elastomer to shearing and failure at extreme loading conditions were conducted by Clifton and coworkers [10–12]. The polyurea is cast between two steel plates. The flyer impacts the sandwich plate at high velocity. For pressure-shear tests, the flyer is slightly inclined at angle $\theta = 18°$ to produce a shear response of the polyurea as shown in Fig. 2. We consider two pressure-shear experiments: Shot#1201 and Shot#404 at shear-strain rates of $4.1 \times 10^5\ \mathrm{s}^{-1}$ and $2.4 \times 10^5\ \mathrm{s}^{-1}$, respectively. The main difference between the two shots is impact velocity (see Table 3), which is higher for Shot#1201. In addition, we consider a pure compression experiment, Shot#1203, which is required to identifying pure compression stress-strain relation. The geometry, material properties and impact velocities are described in Tables 2 and 3, (for details see references [10, 11]).

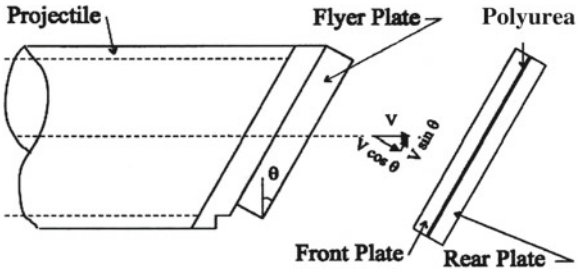

Fig. 2 Experiment setting [10]

Table 2 Flyer and plate steel material parameters

Shot No.	Steel	Density (g/cm^3)	Young's modulus (MPa)	Poisson's ratio
1201, 1203	Pure WC	15.4	609100	0.2
404	Hampden steel	7.861	213700	0.29

Table 3 Thickness of the flyer, sandwich plates, and impact velocity for two experiments

Shot No.	Sample –polyurea (mm)	Front plate (mm)	Rare plate (mm)	Flyer (mm)	Impact velocity V_0 (m/s)	Angle θ (°)
1201	0.097	3.582	5.578	7.411	183.45	18
1203	0.089	3.588	5.898	10.5	175	0
404	0.11	2.896	7.041	6.991	112.6	18

3.2 Numerical Simulation

For numerical simulations we consider an idealized model: a narrow longitudinal strip (in 3D) of a sandwich and a flyer as shown in Fig. 3. Such an idealization was originally proposed in reference [18]. The polyurea is modeled by one 8-node hexahedral solid element. The flyer and the steel plates were meshed by 8-node hexahedral solid elements and modeled as elastic material with parameters described in Table 2. The boundary and initial conditions are listed in Table 4. The calibrated material parameters of the GVBO model of polyurea are listed in Table 5. The parameter E_m is taken to be the maximum Young's modulus observed in Shot#404. The parameters $k_1, \ldots, k_4$ and p are calibrated against the experimental data from Shots#1201 and #404. Note that we use the same set of polyurea parameters for both experiments in Shot#1201 and Shot#404.

We also consider cohesive elements at the interfaces between the polymer layer and the steel. The cohesive element is described by an anisotropic traction-separation law. The damage initiates at a maximum effective stress, and the total damage corresponds to the maximum effective displacement as shown in Table 6 . We use different parameters for the cohesive layer in the experiments Shot#1201 and Shot#404 since

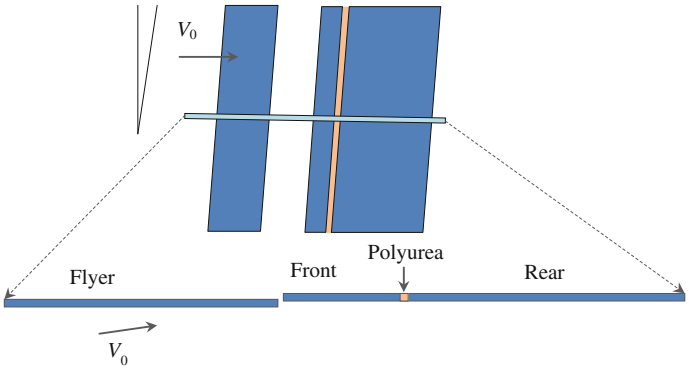

Fig. 3 Simplified numerical simulation model [18]

Table 4 Boundary and initial conditions considered in numerical simulation

Flyer plate	Sandwich plate assembly
Initial velocity: $V_1 = V_0 \cos\theta$, $V_2 = V_0 \sin\theta$	Constraints: $u_1 = \text{free}$, $u_{2\_top} = u_{2\_bottom}$, $u_3 = 0$
Constraints: $u_{2\_top} = u_{2\_bottom}$; $u_3 = 0$	

Table 5 GVBO material parameters for polyurea

Density (g/cm^3)	E_0 (MPa)	ν_0	E_t (MPa)	p	a_1 (MPa)	a_2 (MPa)	a_3 (1/MPa)
1.1	278	0.491	23.3	−6	0	10	0
k_1	k_2 (MPa)	k_3 (MPa)	k_4	E_m (MPa)	A_0 (MPa)	A_c (s^{-1})	A_f (MPa)
17	0.47	1.47	4	13600	1	0	0

Table 6 Material parameters for cohesive interface modeled by traction-separation law

Shot No.	Density (g/cm^3)	Elastic properties (MPa)			Maximum nominal stress (MPa)			Maximum effective displacement (mm)
		E	G_1	G_2	S_n	S_1	S_2	
1201, 1203	1.56	12000	14000	14000	6000	7000	7000	0.8
404	1.56	175	175	175	120	120	120	0.8

the steel plates are different. The presence of the cohesive layer does not influence significantly the numerical results.

The comparison of numerical simulation against experimental data of Shot#1201 is depicted in Figs. 4 and 5. The simulation results can be seen to be in good agreement with the experiments except for the normal velocity that behaves differently after the

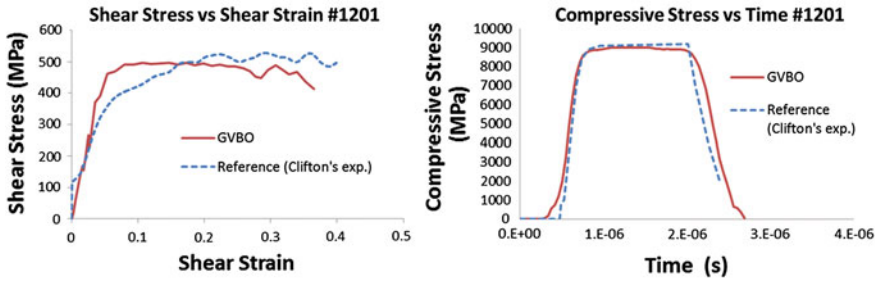

Fig. 4 Shear and compressive stress versus shear strain and time, respectively, for Shot#1201

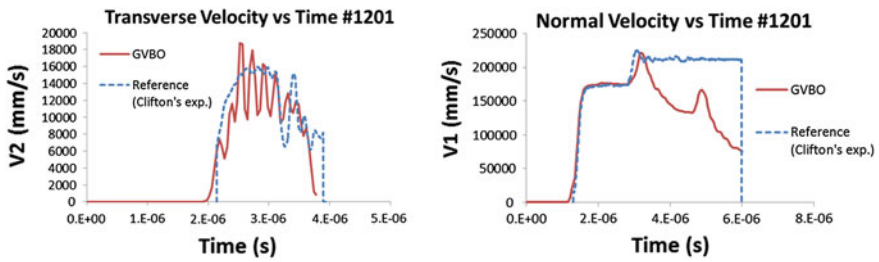

Fig. 5 Transverse and normal velocity versus time for Shot#1201

first peak. This is most likely related to the arrival of the boundary wave and the use of idealized geometry considered in the simulations.

It can be seen that for Shot#404 numerical results are in good agreement with the experimental results (see Figs. 6, 7, 8 (right)).

The compressive stress-strain curve related to pure compression loading-unloading experiments (Shot#1203) is plotted in Fig. 8 (left). The loading compressive stress-strain curve for Shot#404 is depicted in Fig. 8 (right) and compared with the experimental observations taken from reference [11].

The pressure dependence of shearing resistance is approximated by a linear function in Fig. 9 (left), [10]. The numerical simulation results shown in Fig. 9 (right) correspond to the problem geometry and steel material taken from Shot#1201 and Shot#404 (Table 2). The results are obtained for impact velocities ranging between $V_0 = 112.6\,\text{m/s}$ and $V_0 = 183.45\,\text{m/s}$, and fit nicely the linear function predicted by the experiments.

3.3 Confined Monotonic Loading

There is a lack of experimental data for uniaxial monotonic compressive loading at strain rates in the range of about $10^5\,\text{s}^{-1}$ and in the presence of large distortions. Instead, we consider experimental data from reference [18] related to confined com-

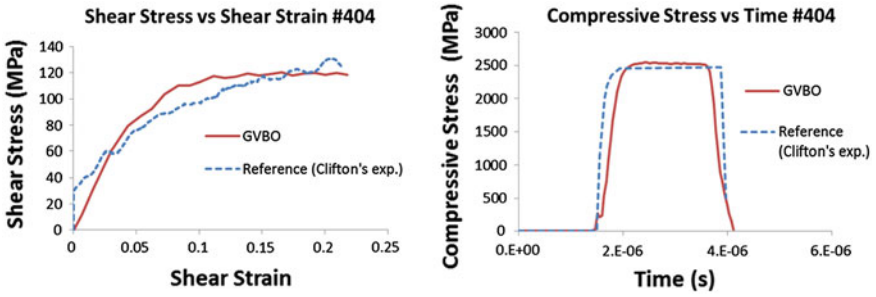

Fig. 6 Shear and compressive stress versus shear strain and time, respectively, for Shot#404

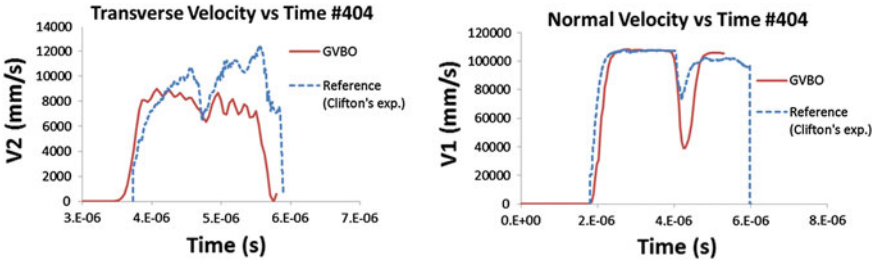

Fig. 7 Transverse and normal velocity versus time for Shot#404

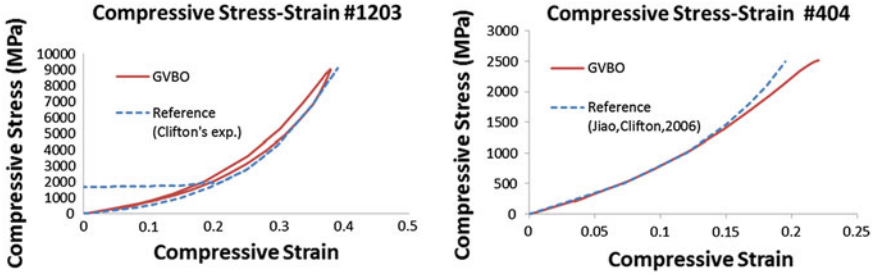

Fig. 8 Compressive stress versus compressive strain for pure-compression Shot#1203 (*left*) and for pressure-shear Shot#404 [11] (*right*)

pressive test of polyurea subjected to a strain rate of $2600\,s^{-1}$ at 273 K. We model confined compression for a single element of polyurea. Figure 10 shows a reasonable agreement with experimental data. The result has been found to be almost insensitive to inelastic material parameters.

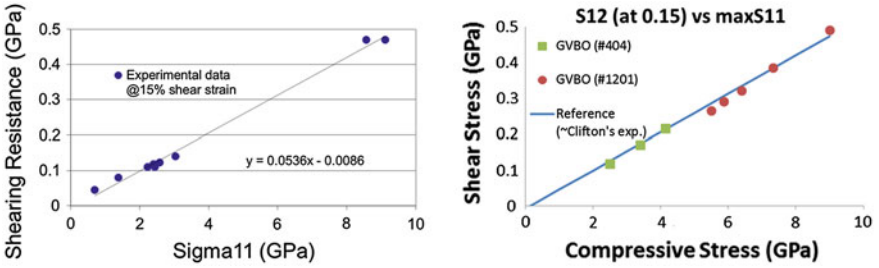

Fig. 9 Dependence of shear resistance on pressure: experimental data [2] (*left*) and numerical simulations (*right*)

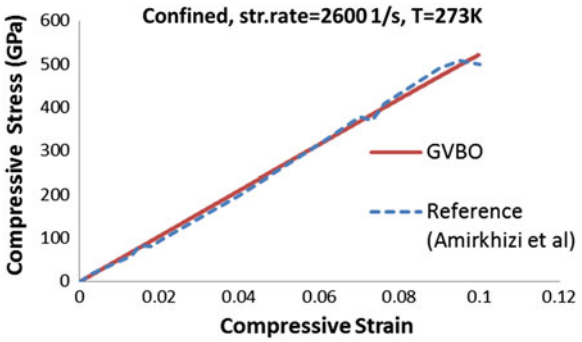

Fig. 10 Confined compressive stress-strain curves for GVBO and experimental data [18]

3.4 Validation for Polyurea/Steel Bi-Layer

In this section we consider a composite polyurea/steel plate impacted by FSP (fragment simulating projectile) at very high velocities (>1000 m/s). Two positions of the polymer layer with respect to the steel have been considered: the front and back coating, with a front side being the target.

The polyurea is modeled by the generalized viscoplasticity model based on overstress (GVBO) outlined in the previous section. For failure criterion, we considered the maximum principal strain. For high-hard steels we studied MIL-A46100 steel which is modeled by the Johnson-Cook constitutive model.

The ballistic limit (or V_{50} velocity) is estimated for a blank steel plate, polyurea-steel plate and steel-polyurea plate. It has been observed that the bi-layer with a front polyurea coating increases penetration velocity by about 15.4 %, while the plate with back coating raises penetration velocity by only 7.5 % for MIL-A46100 steel with respect to the ballistic limit of the blank steel plate.

The polyurea material is modeled by the generalized viscoplasticity model based on overstress. The calibrated material parameters are shown in Table 5. The failure

Table 7 Physical properties of the steel

Steel	Young's Modulus (MPa)	Poisson ratio	Density (g/cm^3)	Inelastic heat fraction, χ	Specific heat (μJ/kgK)	Coefficient of linear thermal expansion (1/K)
MIL-A46100	215000	0.29	7.85	0.9	4.8e+08	11.5e-6

Table 8 The Johnson-Cook parameters for the steel [19, 21]

Steel	A (MPa)	B (MPa)	n	$\dot{\varepsilon}_0$ (s^{-1})	C	m	T_0 (K)	T_m (K)
MIL-A46100	1050	250	0.12	1	0.02	0.5	298	1720

criterion for the polyurea is a maximum principal strain, and the critical damage value is $D^{pol} = 1.4$.

Material properties for the MIL-A46100 steel [19] are listed in Table 7. The parameter χ is the Taylor-Quinney empirical coefficient that represents proportion of plastic work converted into heat, and the value 0.9 is considered in this study following the reference [20].

The steel is modeled by the Johnson-Cook model with material constants taken from references [21, 22]. The von Mises tensile flow stress is defined by

$$\sigma = \left[A + B\varepsilon^n\right]\left[1 + C\ln\dot{\varepsilon}^*\right]\left[1 - T^{*m}\right] \tag{18}$$

where ε is the equivalent (or effective) plastic strain, $\dot{\varepsilon}$ and $\dot{\varepsilon}_0$ are the current and reference strain rates; $\dot{\varepsilon}^* = \dot{\varepsilon}/\dot{\varepsilon}_0$ is the dimensionless plastic strain rate for $\dot{\varepsilon}_0 = 1.0\,\mathrm{s}^{-1}$. The homologous temperature T^* is defined as

$$T^* = \frac{T - T_0}{T_m - T_0} \tag{19}$$

where T_m and T_0 are the melting and room temperatures, respectively. The Johnson-Cook parameters for the steel are summarized in Table 8.

The Johnson-Cook model defines the damage variable as

$$D = \sum \frac{\Delta\varepsilon}{\varepsilon^f} \tag{20}$$

where $\Delta\varepsilon$ is an increment of equivalent plastic strain, and ε^f is the equivalent strain to fracture determined as

$$\varepsilon^f = \left[D_1 + D_2\exp\left(D_3\sigma^*\right)\right]\left[1 + D_4\ln\dot{\varepsilon}^*\right]\left[1 + D_5T^*\right] \tag{21}$$

For the Johnson-Cook model, fracture is assumed to occur when $D = D^{steel} = 1$. The Johnson-Cook failure parameters for the MIL-A46100 steel are not available in

Table 9 The Johnson-Cook failure parameters for the 4340 steel [22]

D_1	D_2	D_3	D_4	D_5
0.05	3.44	−2.12	0.002	0.61

Table 10 Ballistic limit of different plates

Steel	Ballistic limit	Blank steel	Polyurea-steel	Steel-polyurea
High-hard steel, experiments [13, 14]	V_{50} (m/s)	1184 ± 5	1483 ± 7	–
	Difference w.r.t. to blank steel	–	23 %	~ 8.8 %
MIL-A46100, simulation	V_{50} (m/s)	1188	1371 ± 1	1277
	Difference w.r.t. to blank steel	–	15.4 %	7.5 %

the open literature and have been assumed to be the same as for the 4340 steel, (see Table 9 [22]).

The 3D plate is constructed from two layers: steel and polyurea of thickness 12.7 mm. The plate radius considered in the simulations is 125 mm. We consider the impact by a fragment simulating projectile of 0.5 caliber, 12.7 diameter, and mass of 12.4 g.

The impact problem is simulated using Abaqus/Explicit solver with built-in Johnson-Cook material and failure models and the user-defined material subroutine (describing GVBO) for the polyurea. Only one quarter of the plate was simulated assuming its symmetry. The bullet is modeled as a rigid body. The plate is assumed to be free.

The model was meshed using 8-node hexahedral element with reduced integration. For stabilization in Abaqus/Explicit, linear and quadratic bulk viscosity parameters were chosen as 0.54 and 2.4, respectively.

The ballistic limit (V_{50}) is estimated in the simulation as an average velocity between the minimum impact velocity for penetration and maximum velocity before penetration. It is listed in Table 10 for the blank steel and coated steel plates. These simulation results are comparable with the results obtained in the experiments [13, 14]. The difference in the ballistic limit between the polyurea-steel and the blank steel is about 15.4 %.

Note that the enhancement obtained by the front polyurea layer is slightly smaller than in the numerical simulation reported in [23] (where an impact problem of FSP penetrating polyurea-4340 steel was considered, and the polyurea was modeled using different viscoplasticity model [15]). In reference [23], the ballistic limits of the blank steel plate and the polyurea-steel bi-layer were overestimated.

Figure 11 shows the snapshot of a projectile penetration into the bi-layer of polyurea and MIL-A46100 steel at impact velocity of $V = 1370$ m/s. The figure compares the relative position of the projectile in the polyurea layer in front and back

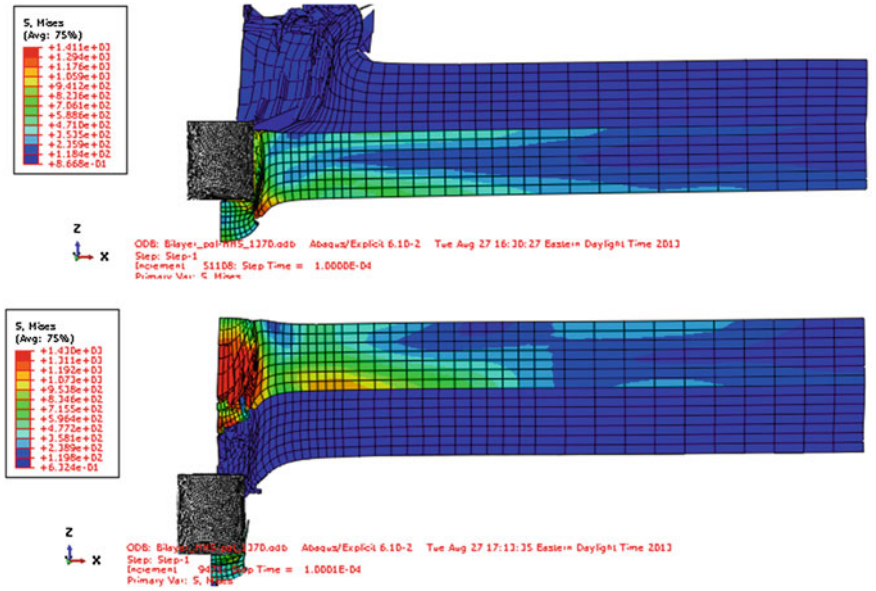

Fig. 11 The FSP impact on polyurea-MIL-A46100 steel plate (*top*) and MIL-A46100 steel-polyurea plate (*bottom*) at impact velocity of 1370 m/s at time 1.e-04s

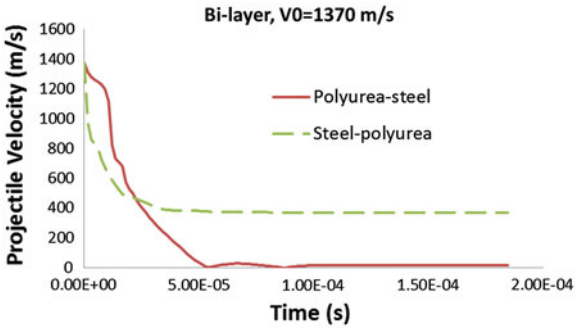

Fig. 12 FSP velocity for polyurea-steel and steel-polyurea plates at impact velocity of 1370 m/s

coating configurations. The results suggest a delay in the projectile penetration in the case of the front polyurea coating polyurea in comparison to the back coating.

The evolution of the projectile velocity in time for both composite plate configurations is shown in Fig. 12. It can be seen that the decrease in the projectile velocity is more pronounced in the case of front polyurea coating of the steel.

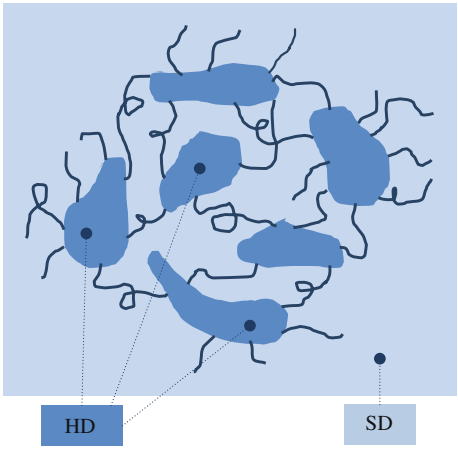

Fig. 13 Micromechanical model of polyurethane consisting of hard domains (HD) and soft domains (SD) with a low HD content [25]

4 Multiscale Modeling of Polymer

4.1 Block Copolymers

Microstructure of the polyurea is composed of hard domains (HD) and soft domain (SD) forming a two-phase microstructure as shown in Fig. 13. Hard segments are with high glass-transition temperature T_g and soft segments are with low T_g. The soft segment has its glass transition below the normal operating temperature and is, therefore, rubbery. The hard segment has its glass transition or its melting temperature above the ordinary operating temperature and is, therefore, either glassy and/or crystalline. It is well known that the microphase separation of hard and soft domains is responsible for the versatile properties of this broad class of polymers [24, 25]. Recent studies [26] have shown that T_g of the soft domain is on average 80 °C higher at the free surface than in the interior and 60 °C higher than at the circumference. For the low strain rate tensile specimens, the T_g increases with strain and reaches a maximum value at a strain of 3.6. These increases in the glass transition temperatures is believed to be due to mixing of the hard and soft segments, but the precise mechanism is not well understood and cannot be investigated without performing micromechanical analysis of the polymer.

Numerous experimental studies (see for example [27]) suggested a significant shift in glass transition T_g with strain rate. The precise effect of strain rate on hard and soft domains is not known, except on the overall behavior of the polymer. We will identify the rate dependent properties of SD and HD domain using inverse method.

4.2 Multiscale Model of Copolymers

Consider the following governing equations of a block copolymer over the composite domain Ω^ζ

$$\begin{aligned}
\sigma^\zeta_{ij,j} + b^\zeta_i &= \rho^\zeta \ddot{u}^\zeta_i \quad \text{on} \quad \Omega^\zeta \\
\Delta\sigma^\zeta_{ij} &= L^\zeta_{ijkl}\left(\Delta\varepsilon^\zeta_{kl} - \Delta\mu^\zeta_{kl}\right) \quad \text{on} \quad \Omega^\zeta \\
\Delta\varepsilon^\zeta_{ij} &= \Delta u^\zeta_{(i,j)} \equiv \frac{1}{2}\left(\Delta u^\zeta_{i,j} + \Delta u^\zeta_{j,i}\right) \quad \text{on} \quad \Omega^\zeta \\
u^\zeta_i &= \bar{u}^\zeta_i \quad \text{on} \quad \Omega^{u\zeta} \\
\sigma^\zeta_{ij} n^\zeta_j &= t^\zeta_i \quad \text{on} \quad \Omega^{t\zeta}
\end{aligned} \tag{22}$$

where $\mathbf{u}^\zeta$ is displacement, ρ^ζ is density; $\Delta u^\zeta_{i,j}$ denotes the derivative of displacement increment with respect to the midstep; $\Delta u^\zeta_{(i,j)}$ denotes the symmetric gradient; $\Delta\varepsilon^\zeta_{kl} = \Delta u^\zeta_{(i,j)}$ is an integral of the rate of deformation over the time step; $\boldsymbol{\mu}^\zeta$ is an eigenstrain; and σ^ζ_{ij} is Cauchy stress. The microscopic coordinate system is $\mathbf{y} = \mathbf{x}/\zeta$, and it is considered to be independent on the macroscopic system of coordinates, $\mathbf{x}$, when $\zeta \ll 1$. Then the spatial derivative rule is $\partial_{,i} = \partial_{,x_i} + \partial_{,y_i}/\zeta$.

For a viscoplastic material considered in Sect. 2 undergoing large strains, it is convenient to decompose the eigenstrain increment as follows

$$\begin{aligned}
\Delta\mu^\zeta_{kl} &= \Delta\mu^{in}_{kl} + \Delta\mu^{el}_{kl} \\
\Delta\mu^{el}_{kl} &= \left(I_{klij} - \left(L^\zeta_{klmn}\left(E^\zeta_0, G^\zeta_0\right)\right)^{-1} L^\zeta_{mnij}\left(E^\zeta, G^\zeta\right)\right)\left(\Delta\varepsilon^\zeta_{ij} - \Delta\mu^{in}_{ij}\right)
\end{aligned} \tag{23}$$

where $\Delta\mu^{el}_{kl}$ is contribution to eigenstrain resulting from deformation-dependent elastic properties (16), and $\Delta\mu^{in}_{kl}$ is the usual inelastic strain increment.

The displacement field is expanded asymptotically as

$$u^\zeta_i(\boldsymbol{x}, \boldsymbol{y}, t) = u^c_i(\boldsymbol{x}, t) + \zeta u^{(1)}_i(\boldsymbol{x}, \boldsymbol{y}, t) + O\left(\zeta^2\right) \tag{24}$$

where $\mathbf{u}^c$ and $\mathbf{u}^{(1)}$ are coarse and fine-scale displacements, respectively.

The first order strain field is given by

$$\begin{aligned}
\Delta\varepsilon^\zeta_{ij}(\boldsymbol{x}, \boldsymbol{y}, t) &= \Delta\varepsilon^c_{ij}(\boldsymbol{x}, t) + \Delta u^{(1)}_{(i,y_j)}(\boldsymbol{x}, \boldsymbol{y}, t) + O(\zeta) \\
\Delta\varepsilon^c_{ij}(\boldsymbol{x}, t) &= \Delta u^c_{(i,x_j)}(\boldsymbol{x}, t) = \frac{1}{|\Theta|}\int_\Theta \Delta\varepsilon^\zeta_{ij}(\boldsymbol{x}, \boldsymbol{y}, t)\, d\Theta
\end{aligned} \tag{25}$$

The fine-scale displacement is assumed to be decomposed as [28–32]

$$\Delta u_i^{(1)}(\boldsymbol{x},\boldsymbol{y},t) = H_i^{kl}(\boldsymbol{y},t)\,\Delta\varepsilon_{kl}^{c}(\boldsymbol{x},t) + \int_{\Theta} g_i^{kl}(\boldsymbol{y},\tilde{\boldsymbol{y}},t)\,\Delta\mu_{kl}^{\zeta}(\boldsymbol{x},\tilde{\boldsymbol{y}},t)\,d\tilde{\Theta} \tag{26}$$

where H_i^{kl}, g_i^{kl} are $\boldsymbol{y}$-periodic instantaneous functions for elastic and inelastic deformation, respectively. Note that for large strain problems, the unit cell domain may evolve and therefore the influence functions may change from one increment to another. In the present manuscript we introduce an approximation by which we approximate the influence functions by their initial values

$$\begin{aligned} H_i^{kl}(\boldsymbol{y}) &\equiv H_i^{kl}(\boldsymbol{y},t) = H_i^{kl}(\boldsymbol{y},0) \\ g_i^{kl}(\boldsymbol{y},\tilde{\boldsymbol{y}}) &\equiv g_i^{kl}(\boldsymbol{y},\tilde{\boldsymbol{y}},t) = g_i^{kl}(\boldsymbol{y},\tilde{\boldsymbol{y}},0) \end{aligned} \tag{27}$$

In the model reduction approach [28–33] the eigenstrain field is discretized over volume partitions as follows

$$\mu_{ij}^{\zeta}(\boldsymbol{x},\boldsymbol{y},t) = \sum_{\alpha=1}^{n} N^{(\alpha)}(\boldsymbol{y})\,\mu_{ij}^{c(\alpha)}(\boldsymbol{x},t) \tag{28}$$

where n is a number of partitions or phases. A shape function $N^{(\alpha)}$ is either continuous (for compatible eigenstrains, see [33]) or piece-wise constant as follows

$$N^{(\alpha)}(\boldsymbol{y}) = \begin{cases} 1 & \boldsymbol{y} \in \Theta^{(\alpha)} \\ 0 & \boldsymbol{y} \notin \Theta^{(\alpha)} \end{cases} \quad \bigcup_{\alpha=1}^{n} \Theta^{(\alpha)} = \Theta; \quad \bigcap_{\alpha=1}^{n} \Theta^{(\alpha)} = \emptyset \tag{29}$$

and

$$\mu_{ij}^{c(\beta)}(\boldsymbol{x},t) = \frac{1}{\left|\Theta^{(\beta)}\right|} \int_{\Theta^{(\beta)}} \mu_{kl}^{\zeta}(\boldsymbol{x},\boldsymbol{y},t)\,d\Theta^{(\beta)} \tag{30}$$

Inserting (27) and (28) into (26) and introducing $S_i^{kl(\alpha)}(y) = \int_{\Theta} g_i^{kl}(\boldsymbol{y},\tilde{\boldsymbol{y}})\,N^{(\alpha)}(\tilde{\boldsymbol{y}})\,d\tilde{\Theta}$ yields

$$\Delta u_i^{(1)}(\boldsymbol{x},\boldsymbol{y},t) = H_i^{kl}(\boldsymbol{y})\,\Delta\varepsilon_{kl}^{c}(\boldsymbol{x},t) + \sum_{\alpha=1}^{n} S_i^{kl(\alpha)}(\boldsymbol{y})\,\Delta\mu_{kl}^{c(\alpha)}(\boldsymbol{x},t) \tag{31}$$

Inserting (31) into (25) gives

$$\Delta\varepsilon_{kl}^{\zeta}(\boldsymbol{x},\boldsymbol{y},t) = \left(I_{klmn} + H_{(k,y_l)}^{mn}(\boldsymbol{y})\right)\Delta\varepsilon_{mn}^{c}(\boldsymbol{x},t) + \sum_{\alpha=1}^{n} S_{(k,y_l)}^{mn(\alpha)}(\boldsymbol{y})\,\Delta\mu_{mn}^{c(\alpha)}(\boldsymbol{x},t) \tag{32}$$

Given the rate of deformation increment and the previous converged value of Cauchy stress in each phase of the unit cell the stress can be updated using the GVBO model outlined in the previous section.

Finally, the coarse-scale Cauchy stress is obtained by averaging fine-scale stresses

$$\sigma_{ij}^{c} = \frac{1}{|\Theta|}\int_{\Theta} \sigma_{ij}^{\zeta} d\Theta \tag{33}$$

for the coarse-scale equilibrium equation

$$\sigma_{ij,j}^{c} + b_i^c = \rho^c \ddot{u}_i^c \tag{34}$$

where $\mathbf{b}^c$ and ρ^c are averages of fine-scale body force $\mathbf{b}^\zeta$ and density ρ^ζ, respectively.

4.3 Dispersion Contribution

In dynamic multiscale problems there is an effect of micro-inertia, which arises due to material heterogeneity. We account for the micro-inertia effect in the coarse-scale problem by modifying the coarse-scale stress (for more details see [17])

$$\bar{\sigma}_{ij}^{c} = \sigma_{ij}^{c} + \zeta^2 D_{ijkl} \ddot{\varepsilon}_{kl}^{c} \tag{35}$$

The coarse-scale problem (34) is then redefined as

$$\begin{aligned} \bar{\sigma}_{ij,j}^{c} + b_i^c &= \rho^c \ddot{u}_i^c \quad \text{on} \quad \Omega \\ \bar{\sigma}_{ij,j}^{c} n_j^c &= \bar{t}_i^c \quad \text{on} \quad \partial\Omega^t \end{aligned} \tag{36}$$

where D_{ijkl} is a dispersion coefficient that depends on the material impedance, unit cell size and overall density [17].

To compute the dispersion coefficient it is convenient to decompose it to linear and nonlinear contributions

$$D_{ijkl} = D_{ijkl}^{\text{lin}} + D_{ijkl}^{\text{nonlin}} \tag{37}$$

The linear term is defined as

$$D_{ijkl}^{\text{lin}} \equiv \rho^c \frac{1}{|\Theta|}\int_{\Theta} h_s^{ij} h_s^{kl} d\Theta \tag{38}$$

where h_i^{kl} is $\boldsymbol{y}$-periodic solution of the following problem

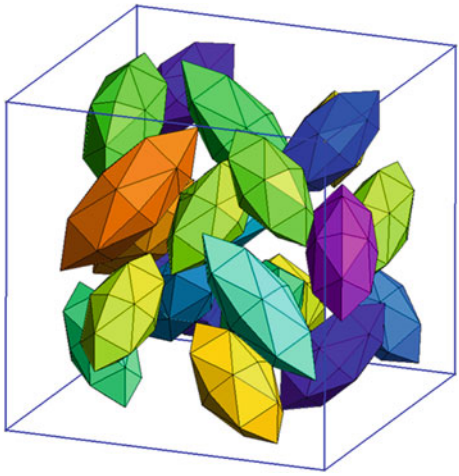

Fig. 14 Microstructure of the unit cell with particles preferentially oriented at a 45° with respect to a vertical axis

$$
\begin{aligned}
&h^{kl}_{(i,y_j)}(y) = H^{kl}_{(i,y_j)}(y) + \tfrac{\Delta\rho(y)}{\rho^c} I_{ijkl} \\
&\int_\Theta h^{ij}_s \, d\Theta = 0;\ \Delta\rho(y) = \rho^c - \rho(y)
\end{aligned}
\tag{39}
$$

The nonlinear term is defined as

$$
\begin{aligned}
D^{\text{nonlin}}_{ijkl} &\equiv \sum_{\alpha=1}^{n}\sum_{\beta=1}^{n} \frac{\partial \Delta\mu^{(\alpha)}_{st}}{\partial \Delta\varepsilon^c_{ij}} R^{(\alpha\beta)}_{stpq} \frac{\partial \Delta\mu^{(\beta)}_{pq}}{\partial \Delta\varepsilon^c_{kl}} + \sum_{\alpha=1}^{n} Q^{(\alpha)}_{ijpq} \frac{\partial \Delta\mu^{(\alpha)}_{pq}}{\partial \Delta\varepsilon^c_{kl}} + \sum_{\alpha=1}^{n} Q^{(\alpha)}_{klpq} \frac{\partial \Delta\mu^{(\alpha)}_{pq}}{\partial \Delta\varepsilon^c_{ij}} \\
R^{(\alpha\beta)}_{stpq} &= \rho^c \frac{1}{|\Theta|} \int_\Theta S^{st(\alpha)}_r S^{pq(\beta)}_r \, d\Theta;\ Q^{(\alpha)}_{ijpq} = \rho^c \frac{1}{|\Theta|} \int_\Theta h^{ij}_r S^{pq(\alpha)}_r \, d\Theta
\end{aligned}
\tag{40}
$$

Note that the dispersion effect becomes significant when (i) the unit cell size is large, (ii) material impedance is considerable (i.e. large difference in elastic moduli or densities between phases) and (iii) spatial gradient of acceleration is high.

5 Verification of the Multiscale Model

For modeling polyurea microstructure, we consider an anisotropic unit cell with ellipsoidal particles (volume fraction 19 %) shown on Fig. 14. The particles are oriented at preferential angle of 45° with respect to the loading direction.

The soft domains are modeled by the GVBO model while hard domains are kept elastic with considerably higher elastic modulus than the initial modulus in the soft domain. Material parameters of the phases (Table 11) are calibrated to the experimental data of normal dynamic impact test [10] and confined test under monotonic

Table 11 GVBO parameters for polyurea in two-scale analysis

Soft domains	E_0 (MPa)	ν_0	E_t (MPa)	p	a_1 (MPa)	a_2 (MPa)	a_3 (1/MPa)
	156	0.494	23.3	−6	0	10	0
k_1	k_2 (MPa)	k_3 (MPa)	k_4	E_m (MPa)	A_0 (MPa)	A_c (s^{-1})	A_f (MPa)
17	0.47	1.47	4	13600	1	0	0
Hard domains	E_0 (MPa)	ν_0					
	890	0.491					

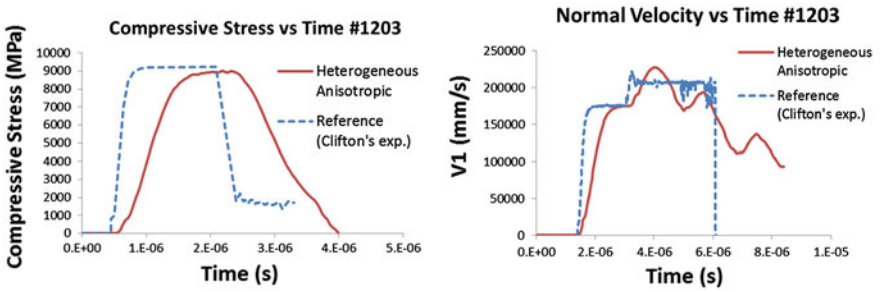

Fig. 15 Compressive stress and normal velocity versus time. Comparison of multiscale simulation with calibrated parameters and experimental data, Shot#1203 [10]

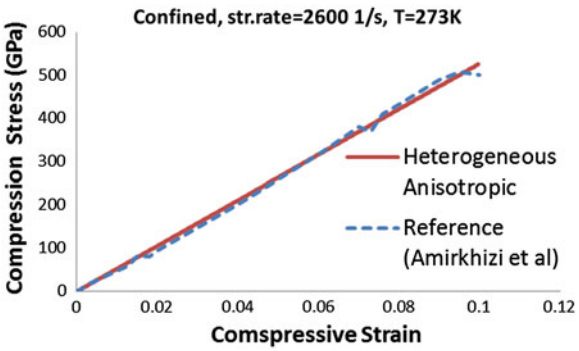

Fig. 16 Confined compressive stress-strain curves. Comparison of multiscale simulation with calibrated parameters and experimental data [18]

compressive loading [18]. The results are shown in Figs. 15 and 16. The two-scale model of polyurea is implemented in Abaqus /Explicit with MDS plugin http://multiscale.biz.

The multiscale model of polyurea is studied for impact problem on polyurea/steel bi-layer and single polyurea layer. In these studies we have not considered material failure and thus relatively low impact velocity have been analyzed.

The evolution of projectile velocity is shown in Figs. 17 and 19 for bi-layer and single layer, respectively. The response of the heterogeneous anisotropic material